

Lindhard and RPA susceptibility computations in extended momentum space in electron doped cuprates

Yung Jui Wang¹, B. Barbiellini¹, Hsin Lin¹, Tanmoy Das¹, Susmita Basak¹,
P.E. Mijnders^{1,2}, S. Kaprzyk^{1,3}, R.S. Markiewicz¹ and A. Bansil¹

¹*Physics Department, Northeastern University,
Boston, Massachusetts 02115, USA*

²*Department of Radiation, Radionuclides & Reactors,
Faculty of Applied Sciences,
Delft University of Technology, Delft, The Netherlands*

³*AGH University of Science and Technology,
30059 Kraków, Poland*

(Dated: August 17, 2012)

We present an approximation for efficient calculation of the Lindhard susceptibility $\chi^L(\mathbf{q}, \omega)$ in a periodic system through the use of simple products of real space functions and the fast Fourier transform (FFT). The method is illustrated by providing $\chi^L(\mathbf{q}, \omega)$ results for the electron doped cuprate $\text{Nd}_{2-x}\text{Ce}_x\text{CuO}_4$ extended over several Brillouin zones. These results are relevant for interpreting inelastic X-ray scattering spectra from cuprates.

PACS numbers: 78.70.Ck

1. INTRODUCTION

The dynamic structure factor $S(\mathbf{q}, \omega)$ is a useful function of momentum and energy introduced by Leon Van Hove¹, which contains information about density-density correlations and their time evolution. Experimentally, $S(\mathbf{q}, \omega)$ can be accessed most directly by Inelastic X-ray Scattering (IXS), which has acquired greater importance with the advent of powerful synchrotron sources². However, since X-rays are strongly absorbed in materials with high density, IXS may be suitable mostly for low- Z systems. Nevertheless, in the case of heavier elements, recent studies have shown that if the photon incident energy is near an X-ray absorption edge the cross section can be enhanced, and the resulting resonant inelastic X-ray scattering (RIXS) offers a new window for probing both empty and filled electronic states³⁻⁵. Recent efforts to develop a first-principles formulation of the RIXS spectrum explore an interesting hypothesis⁶⁻⁸ that the RIXS cross-section is directly related to $S(\mathbf{q}, \omega)$, complicating effects of the core hole notwithstanding. However, this claim remains controversial⁹ and must be checked by testing the theory against accurate experimental results¹⁰. Cu-K-edge RIXS for cuprates^{3,11-13} probes the spectrum throughout momentum space encompassing many Brillouin zones. Therefore an important theoretical task is to produce realistic calculations of the dynamic structure factor within the framework of either Many-Body Perturbation Theory (MBPT) or Time-Dependent Density Functional Theory (TDDFT)¹⁴ starting from a Lindhard susceptibility representing the response of an unperturbed Kohn-Sham system. In particular, local field effects¹⁵⁻¹⁸ are known to modify the spectral weight of both collective and single-particle excitations in the dynamic structure factor of solids.

In this study we focus on an approximation to effi-

ciently calculate from one particle spectral functions the Lindhard susceptibility $\chi^L(\mathbf{q}, \omega)$. This approximation has successfully described the susceptibility of heavy rare earth elements¹⁹ and can also reliably describe the X-ray inelastic scattering momentum dependency in higher Brillouin zones for an energy transfer ω where the single-particle excitations dominate. As an example we consider paramagnetic $\text{Nd}_{2-x}\text{Ce}_x\text{CuO}_4$ (NCCO), which has a relatively simple, nearly two-dimensional metallic Cu-O band near the Fermi level. We identify important features throughout energy-momentum space and we delineate the specific manner in which $\text{Im}\chi^L(\mathbf{q}, \omega)$ decays as a function of \mathbf{q} . These results enable an assessment of the extent to which $S(\mathbf{q}, \omega)$ reproduces the RIXS cross-section in a cuprate via direct comparison of the theory with corresponding experiments in extended regions of the momentum space.

An outline of this paper is as follows. In Section 2, we present the relevant formalism. The details of the electronic structure methods and the numerical schemes are given in Section 3. The theoretical results for $\text{Im}\chi^L(\mathbf{q}, \omega)$ are presented and discussed in Section 4, and the conclusions are summarized in Section 5.

2. FORMALISM

In a periodic solid, the susceptibility becomes¹⁵ a tensor in the reciprocal lattice vector space \mathbf{G} . The fluctuation-dissipation theorem relates the dynamical structure factor $S(\mathbf{q}, \omega)$ to the susceptibility via

$$S(\mathbf{q}, \omega) = -\frac{1}{\pi} \sum_{\mathbf{k}, \mathbf{G}} \frac{\text{Im}[\chi_{\mathbf{G}, \mathbf{G}}(\mathbf{k}, \omega)]}{1 - e^{-\hbar\omega/kT}} \delta(\mathbf{q} - \mathbf{k} - \mathbf{G}). \quad (1)$$

Thus, IXS experiments do not probe all matrix elements of the response $\chi_{\mathbf{G}, \mathbf{G}'}(\mathbf{k}, \omega)$, but only the diagonal ele-

ments $\chi_{\mathbf{G},\mathbf{G}}(\mathbf{k},\omega)^{20}$. If we approximate the susceptibility by the bare susceptibility $\chi_{\mathbf{G},\mathbf{G}}^0(\mathbf{k},\omega)$ then^{16–18,21}

$$\text{Im}[\chi_{\mathbf{G},\mathbf{G}}^0(\mathbf{k},\omega)] = - \sum_{\nu,\mu} |M_{\mathbf{G}}^{\nu,\mu}|^2 \int_{-\omega}^0 d\epsilon A_{\nu}(\epsilon) A_{\mu}(\epsilon + \omega). \quad (2)$$

The matrix elements $M_{\mathbf{G}}^{\nu,\mu}$ can be expressed in the Dyson orbital basis set g_{ν} as^{22,23}

$$M_{\mathbf{G}}^{\nu,\mu} = \langle g_{\nu} | e^{i(\mathbf{k}+\mathbf{G})\cdot\mathbf{r}} | g_{\mu} \rangle. \quad (3)$$

The spectral functions associated with the Dyson orbitals are

$$A(\mathbf{p},\omega) = \sum_{\nu} |g_{\nu}(\mathbf{p})|^2 A_{\nu}(\omega), \quad (4)$$

and

$$A_{\nu}(\omega) = \frac{\gamma}{\pi[(\hbar\omega - \epsilon_{\nu})^2 + \gamma^2]}, \quad (5)$$

where ϵ_{ν} is the excitation energy associated with the Dyson orbital g_{ν} and γ is infinitesimally small (see also Appendix A). The Dyson orbitals can often be approximated reasonably by Bloch orbitals as

$$g_{\mathbf{k},n}(\mathbf{r}) = \exp(i\mathbf{k} \cdot \mathbf{r}) \sum_{\mathbf{G}} C_{\mathbf{G}}^{\mathbf{k},n} \exp(-i\mathbf{G} \cdot \mathbf{r}), \quad (6)$$

with the momentum density given by

$$|g_{\mathbf{k},n}(\mathbf{p})|^2 = \sum_{\mathbf{G}} \delta(\mathbf{p}-\mathbf{k}+\mathbf{G}) |C_{\mathbf{G}}^{\mathbf{k},n}|^2. \quad (7)$$

The label $\nu = (\mathbf{k}, n)$ is a composite index that codes the Bloch wave vector \mathbf{k} and the energy band index n . The Fourier coefficients $C_{\mathbf{G}}^{\mathbf{k},n}$ of the periodic part of the Bloch function are labeled by the reciprocal vectors \mathbf{G} . In this case, the dynamical structure factor at $T = 0$ becomes

$$S(\mathbf{q},\omega) = - \sum_{n,m,\mathbf{k},\mathbf{k}',\mathbf{G}',\mathbf{G}'',\mathbf{G}} (C_{\mathbf{G}'}^{\mathbf{k},n})^* C_{\mathbf{G}'+\mathbf{G}}^{\mathbf{k}',m} C_{\mathbf{G}''}^{\mathbf{k},n} (C_{\mathbf{G}''+\mathbf{G}}^{\mathbf{k}',m})^* \times \delta(\mathbf{q} + \mathbf{k} - \mathbf{k}' - \mathbf{G}) \int_{-\omega}^0 d\epsilon A_n(\mathbf{k},\epsilon) A_m(\mathbf{k}',\epsilon + \omega). \quad (8)$$

The dominant part of $S(\mathbf{q},\omega)$ is given by the partial sum of the real positive terms $\mathbf{G}' = \mathbf{G}''$. Next, following Wen²⁴, we neglect the remaining complex terms because the randomness of their phases produces destructive interferences. A few straightforward algebraic simplifications then yield^{3,25}

$$\text{Im}\chi^L(\mathbf{q},\omega) = - \int_{-\omega}^0 \frac{d\epsilon}{2\pi} \int \frac{d^3p}{(2\pi)^3} A(\mathbf{p},\epsilon) A(\mathbf{p} + \mathbf{q},\epsilon + \omega). \quad (9)$$

Thus, our approximation scheme leads to an expression for $\text{Im}\chi^L(\mathbf{q},\omega)$ similar to the free fermion form²⁶ but

with the spectral function $A(\mathbf{p},\epsilon)$ expressed in terms of the Bloch wave functions instead of plane waves. The approximation of Eq. (9) becomes exact when q is large (see e.g. Ref. [27]). As already noted above, the asymptotic decay of the imaginary part of Lindhard susceptibility as a function of \mathbf{q} is well described within the present framework. When \mathbf{q} is small, the most significant features of the susceptibility are produced by band structure effects, which are fully included in our approach. Notably, the origin of major peaks in the imaginary part of the susceptibility lies in FS nesting.^{28,29} Therefore, we expect our scheme to produce a reasonable approximation to the dynamical structure factor in materials.

3. COMPUTATIONAL METHODS

The Dyson orbitals g_{ν} needed for the calculation of the spectral function $A(\mathbf{p},\epsilon)$, as already noted, can be reasonably replaced by the Kohn Sham orbitals obtained within the Density Functional Theory (DFT)²³. For this purpose, the DFT band structure calculations in NCCO were performed within the Local Density Approximation (LDA) using an all-electron, fully charge self-consistent semi-relativistic (KKR) method³⁰. The crystal structure used for NCCO was body centered tetragonal (space-group I4/mmm) with lattice parameters given by Mas-sidda *et al.*³¹. A self-consistent solution was obtained for $x = 0$ with a convergence of the crystal potential to about 10^{-4} Ry.

To demonstrate our approach in a relatively simple but interesting case, we restrict the calculation to a single band, namely the copper-oxygen band near the Fermi level in NCCO. In particular, the possible contribution of the Nd f-electrons is neglected by removing the f orbital from the basis set after the Nd self-consistent potential has been obtained.³² The electronic structure shown in Fig. 1(a) has been produced with the minority spin part of the self-consistent ferromagnetic potential. The doping effects were treated within a rigid band model by shifting the Fermi energy to accommodate the proper number x of electrons^{33–36}. In the electron momentum density (EMD) calculations (see Ref. 37 for details), the momentum mesh was given by a momentum step $(\Delta p_x, \Delta p_y, \Delta p_z) = (1/128a, 1/128a, 1/2c)/(2\pi)$.^{38–40} The total number of momentum points is 1.54×10^8 \mathbf{p} within a sphere of radius 17.6 a.u.

We show in Fig. 1(a) the calculated band structure of NCCO near the Fermi level. The band closest to the Fermi level is shown by the red dotted curve and is well isolated from other bands. This band ranges from -1.4 eV to 1.9 eV and the integral of the spectral function in this energy interval, evaluated with an energy resolution of 40 meV, is shown in Fig. 1(b). The two-dimensional spectral function $A(\mathbf{p},\omega)$ is calculated by neglecting the small k_z dispersion in the three dimensional electronic band structure⁴¹. Similar EMD results

for NCCO have been obtained within the LMTO^{42,43}. The resulting momentum density has the same symmetry as the copper-oxygen $d_{x^2-y^2} - p_{x,y}$ states in real space which form this energy band since the wave function in momentum space is the Fourier transform of the wave function in real space. Fig. 1(b) shows that the low intensity along the $x-y$ diagonal direction in the 2D-EMD map is a signature of $d_{x^2-y^2}$ symmetry. Moreover, since the radial momentum dependence of an atomic state of angular momentum ℓ behaves as p^ℓ at small momenta⁴⁴, the 2D-EMD intensity at low momenta is from the O-2p orbitals, while the Cu-3d $_{x^2-y^2}$ orbitals contribute at higher momenta.^{45,46} This implies that the signal coming from the O-2p states is more visible in the first Brillouin Zone while the Cu-3d states are better seen in higher Brillouin zones. We can see from Fig. 1(b) that the 2D-EMD intensity is strongly modulated by wave function effects, which suggests that the behavior of $\text{Im}\chi^L(\mathbf{q}, \omega)$ in NCCO in different zones will also be modified by these effects; however, our approximation in Eq. (9) neglects some interference effects produced by the phases of the Fourier coefficients of the Bloch wave functions.

Equation 9 shows that the $\text{Im}\chi^L(\mathbf{q}, \omega)$ at zero temperature can be written as a convolution of two spectral functions. This $\text{Im}\chi^L(\mathbf{q}, \omega)$ captures electron-hole excitations described by Dyson orbitals^{22,23} but does not include collective excitations such as plasmons or phonons. For efficient $\text{Im}\chi^L(\mathbf{q}, \omega)$ calculations, we replace the momentum space convolution of $A(\mathbf{p}, \omega)$ by a simple product of spectral functions $B(\mathbf{r}, \omega)$ in real space given by

$$B(\mathbf{r}, \omega) = \int \frac{d^3p}{(2\pi)^3} A(\mathbf{p}, \omega) \exp(i\mathbf{p} \cdot \mathbf{r}). \quad (10)$$

This enables us to take advantage of the fast Fourier transform (FFT) efficiency using the convolution theorem⁴⁷. The advantage of our FFT based method can be seen by comparing the computation time of the FFT method with the time needed to directly compute $\text{Im}\chi^L(\mathbf{q}, \omega)$ via Eq. 9 using two matrices of size 2049×2049 . The CPU time for the FFT method is 12 seconds, while the direct computation takes 24 minutes on the same machine⁴⁸.

4. RESULTS

We discuss our results with reference to Figures 2-5. In Fig. 2a, we show $-\text{Im}\chi^L(\mathbf{q}, \omega)$ along high symmetry lines as a function of ω . The black part of this figure marks the region of zero intensity where no electron hole transitions are available. Strong intensity seen near 1 eV around $(\pi, 0)$ is due to a sort of a Van Hove singularity in $\text{Im}\chi^L(\mathbf{q}, \omega)$, which is associated with the high energy kink or the waterfall effect in the electronic spectrum⁴⁹. When we compare our Fig. 2a to the experimental RIXS spectrum of overdoped NCCO presented in Ref. 50, we find that the experiment is well described by the \mathbf{k} resolved joint density of states despite the complicating

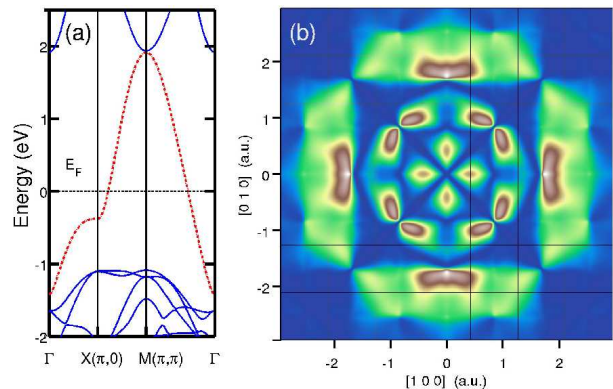


FIG. 1. (Color online) (a) Band structure of NCCO near the Fermi level. The CuO₂ band is shown by the red dotted line. (b) Calculated integrated spectral function $A(\mathbf{p})$ for an isolated CuO₂ layer in NCCO. The zone boundaries (for a simple tetragonal approximation) are marked by black lines. Whites denote large values of $A(\mathbf{p})$, blues small values. The $A(\mathbf{p})$ shown here contain contributions only from the CuO₂ band.

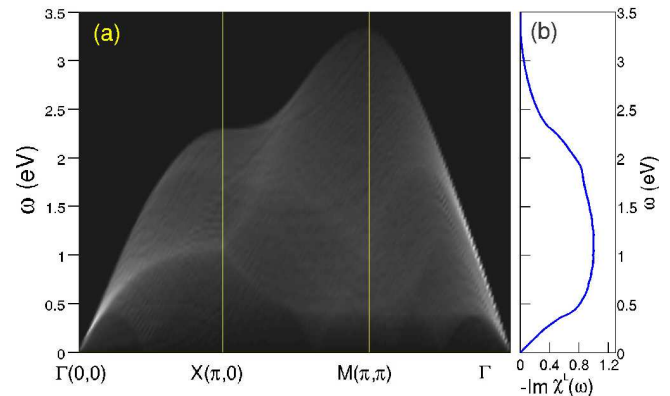


FIG. 2. (Color online) (a) Calculated $-\text{Im}\chi^L(\mathbf{q}, \omega)$ of NCCO along high symmetry lines as a function of transition energy. Whites denote the largest $-\text{Im}\chi^L(\mathbf{q}, \omega)$, blacks the smallest. (b) The integrated value of $-\text{Im}\chi^L(\mathbf{q}, \omega)$ over \mathbf{q} vs transition energy ω .

effects of the core-hole⁸. In particular, the features in the lowest experimental RIXS band within the energy range of $\omega = 0.5$ to $\omega = 2$ eV are well reproduced by our calculations. The integrated value of $-\text{Im}\chi^L(\mathbf{q}, \omega)$ over \mathbf{q} , plotted in Fig. 2b, yields the total number of electron-hole transitions at a given energy. Since the highest peak in Fig. 2b is located at 1.04 eV, we focus on analyzing $-\text{Im}\chi^L(\mathbf{q}, \omega)$ at this particular energy in the remainder of this article. $-\text{Im}\chi^L(\mathbf{q}, \omega)$ is shown in Fig. 3 for $\omega = 1.04$ eV over several Brillouin zones marked by yellow lines. The first Brillouin zone, located at the center of the figure, has the highest intensity. The intensity is seen to decrease slowly as q increases, and interesting patterns due to d electron wavefunction effects appear in higher zones. In the first zone, Fig. 3, some strong peaks are present surrounding the zero-intensity hole centered at

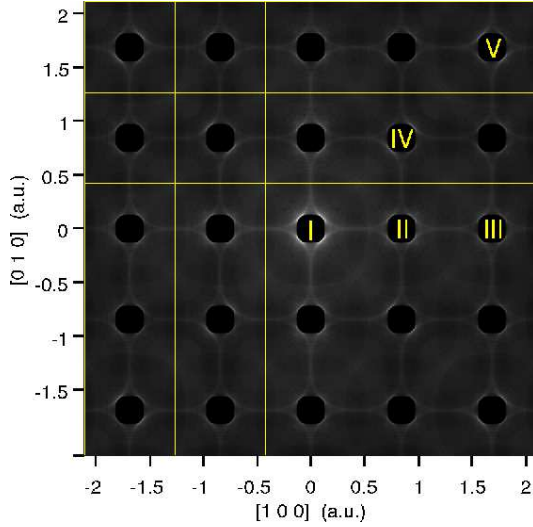


FIG. 3. (Color online) Calculated $-\text{Im}\chi^L(\mathbf{q}, \omega)$ of NCCO at $\omega = 1.04$ eV plotted over several Brillouin zones. Black circles near the Γ -points indicate regions of zero intensity, as in Fig. 2. Index I labels the first zone, indices II, III mark zones along the $(\pi, 0)$ direction, and IV and V the zones along the (π, π) direction.

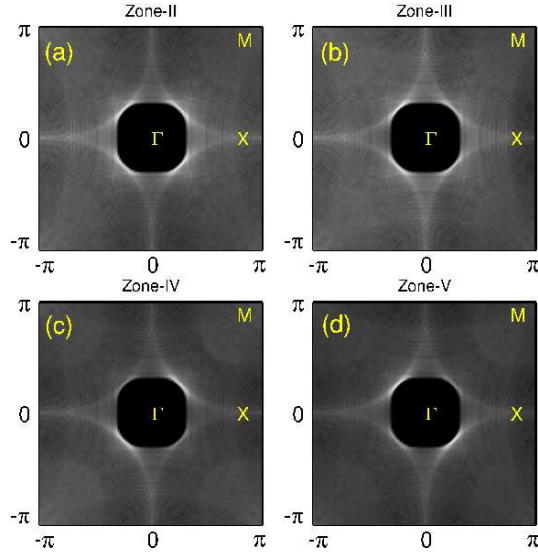


FIG. 4. (Color online) (a-d) Contour maps of $-\text{Im}\chi^L(\mathbf{q}, \omega = 1.04$ eV) of NCCO in four different Brillouin zones. The symmetry of the maps in zone II and zone III is very similar.

Γ with a relatively low intensity appearing at the zone corners M .

Further details of $-\text{Im}\chi^L(\mathbf{q}, \omega)$ are shown in Figs. 4(a)-(d), which are blow ups of the four Brillouin zones marked by II, III, IV, and V in Fig. 3. The Brillouin zones displayed in Figs. 4(a)-(d) show a similar overall pattern but modulated with subtle matrix element effects. For instance, regions of strong intensity spread towards $(-\pi, 0)$ in zone II (Fig. 4a), but towards $(-\pi, \pm\pi)$ in zone III (Fig. 4b). The intense (bright) peaks point along one di-

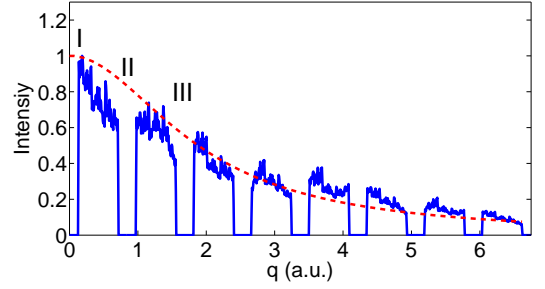


FIG. 5. (Color online) Cuts of $-\text{Im}\chi^L(\mathbf{q}, \omega = 1.04$ eV) taken along $(\pi, 0)$ in Fig. 3 (extended to higher BZs). The highest intensity has been normalized to one. The zone-to-zone change in $-\text{Im}\chi^L(\mathbf{q}, \omega = 1.04$ eV) is mainly an overall decrease in the intensity with smaller changes due to matrix element effects. The envelope of $-\text{Im}\chi^L(\mathbf{q}, \omega)$ is fit by using a simple Lorentzian shape given by the red dashed line. Labels I, II and III correspond to the zone indices in Fig. 3.

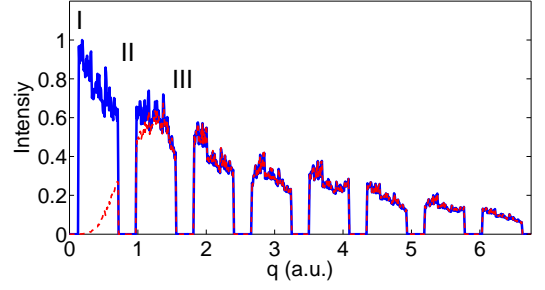


FIG. 6. (Color online) Cuts of $-\text{Im}\chi^{RPA}(\mathbf{q}, \omega = 1.04$ eV) (in red dashed line) and $-\text{Im}\chi^L(\mathbf{q}, \omega)$ (in blue solid line) taken along $(\pi, 0)$ in Fig. 3 (extended to higher BZs). The highest intensity of each curve has been scaled by taking the highest intensity of $-\text{Im}\chi^L(\mathbf{q}, \omega)$ as unity. Labels I, II and III correspond to the zone indices in Fig. 3. No plasmon peak is present in this energy slice $\omega = 1.04$ eV.

agonal direction in zone IV in Fig. 4c, but are rotated by 90 degrees in zone V in Fig. 4d.

Figure 5 presents a cut through $-\text{Im}\chi^L(\mathbf{q}, \omega)$ along the $[100]$ direction in order to illustrate the decay of $-\text{Im}\chi^L(\mathbf{q}, \omega)$ as a function of momentum transfer q . The highest intensity has been normalized to unity for ease of comparison. Surprisingly, at momenta as large as 6 a.u. one can still see features with amplitude exceeding 10 % of the highest intensity (located in the first Brillouin zone). This effect can be explained by the fact that d electron particle-hole transitions can involve particularly high momentum transfers. We can fit the envelope of $-\text{Im}\chi^L(\mathbf{q}, \omega)$ by using a simple Lorentzian shape $\frac{1}{1+(\frac{q}{k_0})^2}$ with $k_0 = 1.89$ a.u.⁵¹ Since RIXS has often been thought to be related to $S(q, \omega)$, it is an interesting question whether a similar decay factor k_0 is found in RIXS experiments. Our results thus provide a new way to test the hypothesis that the RIXS cross-section is directly related to $S(\mathbf{q}, \omega)$.

We have also obtained the real part of Linhard suscep-

tibility χ^L by applying Kramers-Kronig relation. However, the Lindhard susceptibility gives only the response of the independent electrons to the external potential. In order to estimate the effect of screening effects, one can consider the susceptibility within the random phase approximation (RPA) given by $\chi^{RPA} = \chi^L / (1 - V_q \chi^L)$, where V is the Coulomb interaction decaying as $\sim 1/q^2$. In this approach, the sharp singularities of χ^{RPA} due to the denominator give the plasmon modes. Figure 6 illustrates the corrections are more important when the external perturbation is of very long wavelength (i.e. q small)⁵³. Interestingly when q is of the order of k_0 , $-\text{Im}\chi^{RPA}(\mathbf{q}, \omega)$ recovers back to the $-\text{Im}\chi^L(\mathbf{q}, \omega)$.

5. CONCLUSIONS

We have presented a formalism for a first principles computation of the Lindhard susceptibility $\chi^L(\mathbf{q}, \omega)$ in extended momentum space. We have demonstrated a tremendous improvement in performance by calculating $\text{Im}\chi^L(\mathbf{q}, \omega)$ through an approximation involving products of real space spectral functions $B(\mathbf{r}, \omega)$ and FFTs instead of using the standard approach involving costly matrix multiplications. Our theoretical $\text{Im}\chi^L(\mathbf{q}, \omega)$ results for the doped cuprate NCCO will allow a detailed comparison with the RIXS experiments, and hence an assessment of the extent to which $\text{Im}\chi^L(\mathbf{q}, \omega)$ represents a good approximation to the RIXS cross section. The present work also provides a realistic linear response based starting point for developing a many-body perturbation theory of particle-hole excitations within the DFT frame-

work.

We are grateful to J. Lorenzana for discussions. This work is supported by the US Department of Energy, Office of Science, Basic Energy Sciences contracts DE-FG02-07ER46352 and de-sc0007091 (CMCSN), and benefited from the allocation of supercomputer time at NERSC and Northeastern University's Advanced Scientific Computation Center (ASCC). It was also sponsored by the Stichting Nationale Computer Faciliteiten (NCF) for the use of supercomputer facilities, with financial support from NWO (Netherlands Organization for Scientific Research).

Appendix A: Relation between susceptibility and spectral function

We introduce the susceptibility matrix element

$$F^{\nu, \mu} = \frac{f(\epsilon_\nu) - f(\epsilon_\mu)}{\hbar\omega + \epsilon_\nu - \epsilon_\mu + i\gamma}. \quad (\text{A1})$$

where $f(\epsilon)$ is the Fermi function. The term $\text{Im}[F^{\nu, \mu}]$ can be also written in terms of the spectral function A_ν . By using

$$A_\nu(\omega) = \text{Im}\left[\frac{1}{\hbar\omega - \epsilon_\nu + i\gamma}\right], \quad (\text{A2})$$

we obtain

$$\text{Im}[F^{\nu, \mu}] = - \int_{-\omega}^0 d\epsilon A_\nu(\epsilon) A_\mu(\epsilon + \omega). \quad (\text{A3})$$

-
- ¹ L. Van Hove, Phys. Rev. **95**, 249 (1954).
 - ² E. Isaacs and P. Platzman, Physics Today **49**, 40 (February 1996).
 - ³ W. Schülke, Electron Dynamics by Inelastic X-Ray Scattering, Oxford University Press (Oxford 2007).
 - ⁴ A. Kotani and S. Shin, Rev. Mod. Phys. **73**, 203 (2001).
 - ⁵ J.-P. Rueff and A. Shukla, Rev. Mod. Phys. **82**, 847 (2010).
 - ⁶ J. L. J. P. Ament *et al.*, Rev. Mod. Phys. **83**, 705 (2011).
 - ⁷ P. Abbamonte, C. A. Burns, E. D. Isaacs, P. M. Platzman, L. L. Miller, S. W. Cheong, and M. V. Klein, Phys. Rev. Lett. **83**, 860 (1999).
 - ⁸ J. van den Brink and M. van Veenendaal, Europhys. Lett. **73**, 121 (2006).
 - ⁹ R.S. Markiewicz and A. Bansil, Phys. Rev. Lett. **96**, 107005 (2006).
 - ¹⁰ K. H. Ahn, A. J. Fedro, and M. van Veenendaal, Phys. Rev. B **79**, 045103 (2009); C. J. Jia, C.-C. Chen, A. P. Sorini, B. Moritz, and T. P. Devereaux, arXiv:1109.3446v1 [cond-mat.str-el].
 - ¹¹ S. Grenier, J.P. Hill, V. Kiryukhin, W. Ku, Y.-J. Kim, K.J. Thomas, S.-W. Cheong, Y. Tokura, Y. Tomioka, D. Casa, and T. Gog, Phys. Rev. Lett. **94**, 047203 (2005).
 - ¹² Y.J. Kim *et al.*, Phys. Rev. Lett. **89**, 177003 (2002).
 - ¹³ K. Ishii *et al.*, Phys. Rev. Lett. **94**, 207003 (2005).
 - ¹⁴ E. Collart *et al.*, Phys. Rev. Lett. **96**, 157004 (2006).
 - ¹⁵ G. Onida, L. Reining, and A. Rubio, Rev. Mod. Phys. **74**, 601 (2002).
 - ¹⁶ S.L. Adler, Phys. Rev. **126**, 413 (1962).
 - ¹⁷ A. Fleszar, R. Stumpf, and A. G. Eguiluz, Phys. Rev. B **55**, 2068 (1997).
 - ¹⁸ A. Fleszar, A. A. Quong, and A. G. Eguiluz, Phys. Rev. Lett. **74**, 590 (1995).
 - ¹⁹ W. Ku and A. G. Eguiluz, Phys. Rev. Lett. **82**, 2350 (1999).
 - ²⁰ I.D. Hughes *et al.*, Nature, **5**, 446 (2007).
 - ²¹ P. Abbamonte, J. P. Reed, Y. I. Joe, Yu Gan, D. Casa, Phys. Rev. B **80**, 054302 (2009).
 - ²² K. Sturm, Z. Naturforsch. **48a**, 233 (1993).
 - ²³ I. G. Kaplan, B. Barbiellini, A. Bansil, Phys. Rev. B **68**, 235104 (2003).
 - ²⁴ B. Barbiellini, A. Bansil, J. Phys. Chem. Solids **65**, 2031 (2004).
 - ²⁵ See, e.g., Xiao-Gang Wen, *Quantum Field Theory of Many-Body Systems*, Oxford University Press (2004). On page 176, the so-called Wick's theorem approximation is invoked to derive Eq. (4.3.16), which gives the imaginary part of the susceptibility for a system with impurities and/or interactions which break the Galileo invariance.
 - ²⁶ T. K. Ng and B. Dabrowski, Phys. Rev. B **33**, 5358 (1986).
 - ²⁷ Gerald D. Mahan, *Many-Particle Physics*, Springer (2000).

- ²⁷ See e.g. Ref.³ on page 137.
- ²⁸ R.S. Markiewicz, J. Lorenzana, G. Seibold, and A. Bansil, Phys. Rev. B **81**, 014509 (2010).
- ²⁹ C. Utfeld, J. Laverock, T. D. Haynes, S. B. Dugdale, J. A. Duffy, M. W. Butchers, J. W. Taylor, S. R. Giblin, J. G. Analytis, J.-H. Chu, I. R. Fisher, M. Itou, and Y. Sakurai, Phys. Rev. B **81** 064509 (2010).
- ³⁰ A. Bansil, S. Kaprzyk, P.E. Mijnders and J. Toboła, Phys. Rev. B **60**, 13396 (1999); S. Kaprzyk and A. Bansil, Phys. Rev. B **42**, 7358 (1990).
- ³¹ S. Massidda, Jaejun Yu, A.J. Freeman, Physica C **152**, 251 (1988).
- ³² In our LDA calculations, we found a paramagnetic copper layer and a half-metallic ferromagnetic ground state of Nd. To remove the Nd levels from the vicinity of the Fermi level, we simply used the minority spin potential. For a large unit cell, LDA does recover the correct rare earth antiferromagnetic ground state; see T. Jarlborg, B. Barbiellini, H. Lin, R.S. Markiewicz, A. Bansil, Phys. Rev. B **84**, 045109 (2011).
- ³³ N.P. Armitage, P. Fournier and R.L. Greene, Rev. Mod. Phys. **82**, 2421 (2010).
- ³⁴ The rigid band model is expected to be a good approximation for doping away from the cuprate layers. It will however be interesting to examine doping effects by using supercell or other first principles approaches.^{35,36}
- ³⁵ A. Bansil, Zeitschrift Naturforschung A **48**, 165 (1993); H. Asonen *et al.*, Phys. Rev. B **25**, 7075 (1982); R. Prasad and A. Bansil, Phys. Rev. B **21**, 496 (1980); S. N. Khanna, A. K. Ibrahim, S. W. McKnight and A. Bansil, Solid State Commun. **55**, 223 (1985).
- ³⁶ H. Lin, S. Sahrakorpi, R.S. Markiewicz, and A. Bansil, Phys. Rev. Lett. **96**, 097001 (2006).
- ³⁷ P.E. Mijnders and A. Bansil, in *Positron spectroscopy of Solids*, edited by A. Dupasquier and A.P. Mills Jr. (IOS Press, Amsterdam, 1995, p.25).
- ³⁸ EMD can be probed directly via Compton scattering³⁹ or positron-annihilation⁴⁰ experiments.
- ³⁹ Y. Tanaka, Y. Sakurai, A.T. Stewart, N. Shiotani, P.E. Mijnders, S. Kaprzyk, and A. Bansil, Phys. Rev. B **63**, 045120 (2001); S. Huotari, K. Hamalainen, S. Manninen, S. Kaprzyk, A. Bansil, W. Caliebe, T. Buslaps, V. Honkima, and P. Suortti, Phys. Rev. B **62**, 7956 (2000); G. Stutz, F. Wohler, A. Kaprolat, W. Schülke, Y. Sakurai, Y. Tanaka, M. Ito, H. Kawata, N. Shiotani, S. Kaprzyk, and A. Bansil, Phys. Rev. B **60**, 7099 (1999).
- ⁴⁰ P.E. Mijnders, A.C. Kruseman, A. van Veen, H. Schut, and A. Bansil, J. Phys.: Condens. Matter **10**, 10383 (1998); L. C. Smedskjaer, A. Bansil, U. Welp, Y. Fang and K. G. Bailey, Physica C **192**, 259 (1992).
- ⁴¹ R.S. Markiewicz, S. Sahrakorpi, M. Lindroos, Hsin Lin and A. Bansil, Phys. Rev. B **72**, 054519 (2005).
- ⁴² P. Blandin, S. Massidda, B. Barbiellini, T. Jarlborg, P. Lerch, A. A. Manuel, L. Hoffmann, M. Gauthier, W. Sadowski, E. Walker, M. Peter, Jaejun Yu and A. J. Freeman, Phys. Rev. B **46**, 390 (1992).
- ⁴³ B. Barbiellini, S. B. Dugdale and T. Jarlborg, Computational Materials Science **28**, 287 (2003).
- ⁴⁴ P.E. Mijnders, Physica, **63**, 235 (1973).
- ⁴⁵ Similar matrix element effects are seen in angle-resolved photoemission spectra of the cuprates.⁴⁶
- ⁴⁶ M. Lindroos and A. Bansil, Phys. Rev. Lett. **77**, 2985 (1996); A. Bansil, M. Lindroos, S. Sahrakorpi, and R. S. Markiewicz, Phys. Rev. B **71**, 012503 (2005); J. C. Campuzano, L. C. Smedskjaer, R. Benedek, G. Jennings and A. Bansil, Phys. Rev. B **43**, 2788 (1991); M. C. Asensio, J. Avila, L. Roca, A. Tejada, G. D. Gu, M. Lindroos, R. S. Markiewicz, and A. Bansil, Phys. Rev. B **67**, 014519 (2003).
- ⁴⁷ H.N. Rojas, R.W. Godby and R.J. Needs, Phys. Rev. Lett. **74**, 1827 (1995).
- ⁴⁸ The CPU used in the calculations is the Intel Core i7-920.
- ⁴⁹ Susmita Basak, Tanmoy Das, Hsin Lin, J. Nieminen, M. Lindroos, R. S. Markiewicz, and A. Bansil, Phys. Rev. B **80**, 214520 (2009).
- ⁵⁰ Y. W. Li, D. Qian, L. Wray, D. Hsieh, Y. Xia, Y. Kaga, T. Sasagawa, H. Takagi, R. S. Markiewicz, A. Bansil, H. Eisaki, S. Uchida, and M. Z. Hasan, Phys. Rev. B **78**, 073104 (2008).
- ⁵¹ We would like to point out that this fit has no direct consequences for the f-sum rule since it involves only the energy slice $\omega = 1.04$ eV while the f-sum rule is the result of an integration on all the energies. The f-sum rule is automatically fulfilled by our approximation if one neglects self energy corrections and one considers the linear response Lindhard susceptibility (used in this paper) as shown in Ref. 52. Moreover we have numerically checked that $\int \omega \text{Im}\chi^L(\mathbf{q}, \omega = 0) d\omega$ is zero (below 10^{-17}) as a direct consequence of the f-sum rule.
- ⁵² See, e.g. Chapter 3 in G. F. Giuliani and G. Vignale, *Quantum Theory of the Electron Liquid*, Cambridge University Press (2005).
- ⁵³ Interestingly, a full matrix treatment of the susceptibility χ^{RPA} shows that plasmons from the first Brillouin zone can couple with excitations at large momentum transfer. See e.g. R. Hambach, C. Giorgetti, N. Hiraoka, Y. Q. Cai, F. Sottile, A. G. Marinopoulos, F. Bechstedt and Lucia Reining, Phys. Rev. Lett. **101**, 266406 (2008).